Journal of Sol-Gel Science and Technology (2026) 118:7
https://doi.org/10.1007/s10971-026-07148-6

ORIGINAL PAPER

Green and sol-gel synthesis of Cr_2O_3 nanoparticles: comparative photocatalytic degradation of methylene blue using a UV photoreactor

Aiman Waheed[1] · Iqra Muneer[1] · Farhat Yasmeen[1] · Dilawar Ali[2] · Asad Abbas[1] · Farooq Bashir[3] · Aiman Noor Afzal[1]

Received: 21 July 2025 / Accepted: 23 February 2026 / Published online: 24 March 2026
© The Author(s) 2026

Abstract

This study presents a comparative analysis of Cr_2O_3 nanoparticles synthesized by two different methods: a green route using *Cordyline fruticosa* extract (Cr_2O_3-G) and a chemical route via a solvent-controlled sol–gel process with ethanol (Cr_2O_3-C). Their photocatalytic performance in degrading methylene blue (MB) was evaluated under UV irradiation. Comprehensive characterization was performed using FTIR, XRD, UV–vis spectroscopy, particle size analysis, zeta potential measurements, SEM, and EDX to examine structural, optical, and morphological features. Crystallite sizes estimated by the Scherrer equation were 38 nm (Cr_2O_3-G) and 44 nm (Cr_2O_3-C), while Williamson–Hall analysis gave slightly larger values of 48 nm and 58 nm, respectively. Specific surface area (SSA) calculations from XRD indicated a higher SSA for Cr_2O_3-G (30 m^2/g) compared to Cr_2O_3-C (26 m^2/g). The optical band gap was slightly lower for Cr_2O_3-G (3.05 eV) than for Cr_2O_3-C (3.07 eV). Zeta potential values showed better stability for Cr_2O_3-G (–44.3 mV) than Cr_2O_3-C (–21.8 mV). SEM analysis revealed hexagonal structures in Cr_2O_3-G and cubic structures in Cr_2O_3-C. Both catalysts demonstrated excellent photocatalytic activity, achieving nearly complete MB degradation within 20 minutes (97% for Cr_2O_3-G and 96% for Cr_2O_3-C). Although their efficiencies were comparable, notable differences in stability, morphology, surface area, and band gap highlight the strong influence of synthesis methods on the physicochemical properties of Cr_2O_3 nanoparticles.

✉ Iqra Muneer
iqra.muneer@uet.edu.pk

✉ Farhat Yasmeen
f.yasmeen@uet.edu.pk

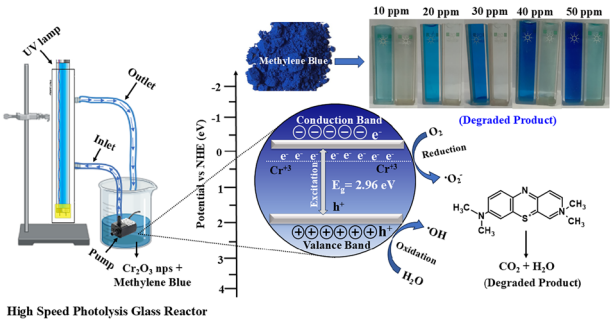
✉ Dilawar Ali
dilawarali@gcu.edu.pk

[1] Department of Chemistry, University of Engineering and Technology, Lahore, Pakistan

[2] Department of Physics, Government College University Lahore, Lahore, Pakistan

[3] Central Research Laboratories, LCW University, Laahore, Pakistan

Graphical Abstract



Keywords Cr_2O_3 nanoparticles · green synthesis · Sol-gel method · UV photoreactor · Surface area · Wastewater treatment

Highlights

- Green and sol–gel methods produced pure rhombohedral Cr_2O_3 nanoparticles.
- Cr_2O_3-G showed a smaller size, a higher surface area, and better stability.
- Dual band gaps enabled efficient UV photocatalysis.
- 97% methylene blue degradation achieved in 20 min (10 ppm).
- Catalysts were reusable; holes (h^+) were the dominant active species.

1 Introduction

The rapid growth of the global population, the intensification of climate change, and the acceleration of industrial development have significantly increased the demand for water. At the same time, contamination of water resources remains a persistent environmental challenge. Industrial effluents containing hazardous organic solvents, dyes, and pathogenic microorganisms pose a serious global concern. Among various sectors, the textile industry is one of the largest contributors to water pollution, frequently discharging dye-laden wastewater into rivers and lakes [1–3].

Methylene blue (MB), a dye widely used in cotton, wool, and paper processing as well as paper stock coating, is of particular concern. Despite its extensive industrial applications, MB is toxic and can cause skin, eye, and respiratory irritation. Moreover, prolonged exposure has been associated with carcinogenic, neurotoxic, and chronic toxic effects in both humans and animals. Alongside chemical pollutants, microbial contamination in water bodies also presents a major challenge to public health and environmental safety [1–5]. As a result, the development of effective water purification strategies has become an urgent global priority.

A variety of treatment methods have been explored for dye removal from wastewater, including reverse osmosis (RO), coagulation, oxidation, photodegradation, filtration, precipitation, adsorption, ion exchange extraction, nanofiltration, ozonation, and electrochemical processes [6]. However, these conventional approaches are often limited by high operational costs, excessive energy consumption, secondary sludge generation, and the reliance on large amounts of chemicals [6, 7]. In contrast, photocatalytic treatment has gained increasing attention as a promising alternative due to its high efficiency, low cost, environmental friendliness, and ease of implementation [4, 5, 8].

Heterogeneous photocatalysis, in particular, provides a safe and efficient means of degrading dyes without generating harmful by-products. Metal oxide nanoparticles such as ZnO, Cr_2O_3, Fe_2O_3 CaO, TiO_2, Cu_2O, and CeO_2, have been widely investigated for wastewater treatment due to their strong catalytic activity in dye degradation [1, 3–5, 9]. Among various metal oxide nanoparticles, Cr_2O_3 NPs are particularly promising due to their distinctive physicochemical properties, wide band gap (3.9 eV), and exceptional durability [3]. They effectively utilize UV light to generate reactive oxygen species that degrade harmful organic pollutants, such as dyes, into harmless byproducts [3]. Their stability and efficiency make them well-suited for cost-effective and sustainable remediation technologies.

Most photocatalytic processes are carried out under UV or visible light using conventional batch systems (e.g., UV rods, beakers, and exhaust fans) [1, 3–5, 9]. However, such batch setups are often inefficient for continuous treatment. To overcome this limitation, we employed a custom-designed UV photoreactor tailored for continuous dye degradation using methylene blue as a model pollutant. Unlike conventional systems, this photoreactor ensures controlled irradiation conditions, uniform light distribution, wavelength specificity, and reproducible exposure. These

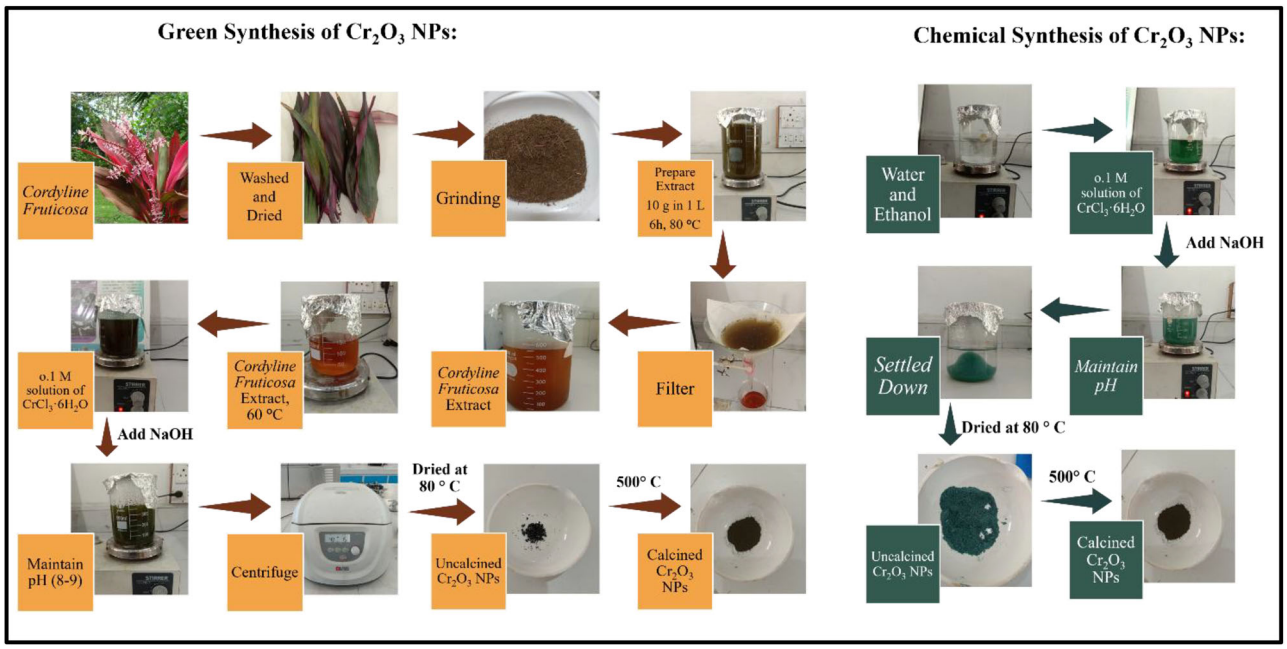


Fig. 1 Preparation of Cr_2O_3-G NPs using Cordyline fruticosa and Cr_2O_3-C NPs through the sol-gel method with ethanol as a capping agent

features minimize external variability, thereby enabling a more reliable evaluation of photocatalytic performance [10].

In this work, Cr_2O_3 nanoparticles were synthesized using both green and chemical approaches. For green synthesis, *Cordyline fruticosa* plant extract was utilized as a capping and stabilizing agent due to its rich bioactive constituents, including flavonoids and saponins [11]. These natural compounds not only support sustainable nanoparticle production but also enhance stability, prevent agglomeration, and improve photocatalytic activity through their antioxidant and antimicrobial functions [12]. For comparison, the sol–gel method was employed as a chemical synthesis route, where chemical solvents served as stabilizers.

2 Experimental Method

2.1 Reagents

Highly purified, analytical-grade reagents (>99.0% purity, Sigma-Aldrich©) were used for the green and chemical synthesis of Cr_2O_3 nanoparticles. The chemical reagents employed in the synthesis included chromium (III) chloride hexahydrate ($CrCl_3 \cdot 6H_2O$), sodium hydroxide (NaOH) for pH adjustment, and ethanol (C_2H_5OH) for chemical synthesis. All experiments were carried out using distilled water. A fresh botanical sample of *Cordyline fruticosa* used in this research was collected from the University of Engineering and Technology, Lahore.

2.2 Preparation of Cordyline fruticosa extract

Cordyline fruticosa leaves were washed with distilled water, dried in an oven at 80 °C for 15 minutes, and ground into powder. 10 g of the powder was mixed with 1 L of distilled water, heated at 80 °C for 3 hours, then stirred at room temperature for another 3 hours. The mixture was filtered to obtain the distilled water extract for further experiments.

2.3 Green synthesis of Cr_2O_3

The green synthesis of Cr_2O_3 nanoparticles, illustrated in Fig. 1, involved preparing a 0.1 M solution by dissolving an appropriate amount of $CrCl_3 \cdot 6H_2O$ in 100 mL of *Cordyline fruticosa* extract, followed by heating and continuous magnetic stirring at 60 °C. The pH was adjusted to 8 using 1 M NaOH, and a color change from brown to green confirmed the formation of the nanoparticles. The mixture was centrifuged at 4000 rpm for 15 minutes, washed thoroughly, dried at 80 °C, and calcined at 500 °C for three hours to obtain the Cr_2O_3 nanoparticles.

2.4 Chemical synthesis of Cr_2O_3 nanoparticles

The chemical synthesis of Cr_2O_3 nanoparticles was performed using a solvent-controlled sol-gel method, as shown in Fig. 1. A 1:5 mole ratio of the chromium precursor to ethanol was stirred at room temperature. The pH was gradually adjusted to 8 by adding 1 M NaOH every 5 minutes

under continuous stirring, leading to a color change from green to bluish-green, indicating the formation of nanoparticles. After 2 hours of stirring, a gel-like material was formed. This gel was centrifuged at 4000 rpm for 15 minutes, thoroughly washed, dried at 80 °C, and calcined at 500 °C for 3 hours to produce the Cr_2O_3 nanoparticles.

2.5 Characterization

The synthesized Cr_2O_3 NPs were characterized using various techniques. UV-Vis absorbance spectra were recorded with an Agilent Cary 60 spectrophotometer. Functional groups were identified through FTIR analysis in the range of 400–4000 cm^{-1}. XRD analysis was conducted using a Rigaku Miniflex 600 diffractometer with Cu Kα radiation (λ = 1.54178 Å), scanning samples in the 2θ range of 20° to 80° at a rate of 2°/min. Morphological and elemental analyses were performed using an FEI NOVA 450 SEM equipped with EDX. Particle size and zeta potential were measured using an Anton Paar Litesizer DLS 500.

2.6 Photocatalytic degradation

The experimental setup for the MB dye removal process using photocatalysis consisted of a Phillips TUV 15 W rod located 1 cm from the reactor and a UV-Vis spectrometer [10]. In each experiment, 0.02 g of Cr_2O_3 nanoparticles (Cr_2O_3-G NPs and Cr_2O_3-C NPs) were separately mixed with aqueous solutions (1000 mL) of methylene blue (MB) dye at varying concentrations (10, 20, 30, 40, and 50 ppm). A control experiment was also performed, where no catalyst was used. Before UV irradiation, the photocatalyst was added to the MB solution, and the mixture was magnetically stirred in the dark to achieve equilibrium. The setup involved pumping the dye solution from the bottom of the beaker, flowing it upward around a glass rod housing the UV lamp, and then exiting through an outlet pipe at the top. The degraded solution was recirculated back to the bottom of the beaker, ensuring consistent exposure to UV light and continuous oxidation of the dye. Absorbance at 664 nm was recorded every 5 minutes to monitor the degradation. The degradation efficiency (%D) was evaluated using Eq. (1).

$$\text{Degradation}(\%) = \left(\frac{A_0 - A_t}{A_0}\right) \times 100 \quad (1)$$

2.7 Scavenger experiments

To identify the role of reactive oxygen species (ROS) in MB degradation, scavenger studies were performed under identical conditions (10 ppm MB, 0.02 g catalyst). Specific quenchers were added to the dye solution before irradiation:

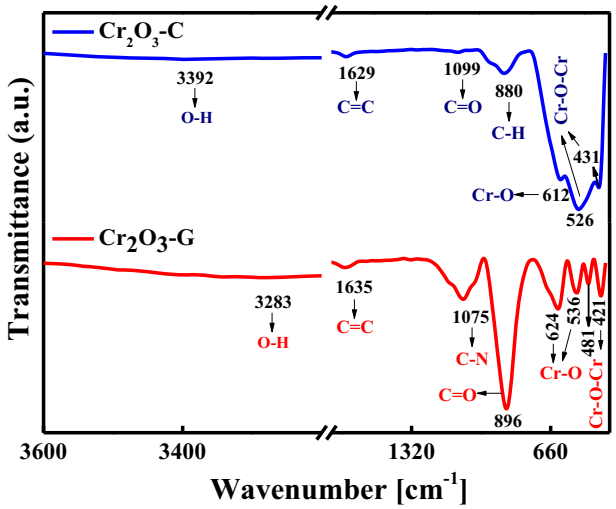


Fig. 2 FTIR spectra of Cr_2O_3 NPs synthesized via green and sol-gel methods

isopropanol (IPA, 1 mM) for hydroxyl radicals (•OH), dimethyl sulfoxide (DMSO, 1 mM) for electrons (e^-), ascorbic acid (AA, 1 mM) for superoxide radicals ($•O_2^-$), and ammonium oxalate (AO, 1 mM) for holes (h^+). The decrease in photocatalytic efficiency compared to the scavenger-free reaction was used to evaluate the dominant ROS involved in the degradation process.

3 Result and discussion

3.1 Fourier Transform Infrared Spectroscopy (FTIR)

FTIR spectroscopy (Fig. 2) was employed to identify functional groups and analyze vibrational modes in Cr_2O_3-G and Cr_2O_3-C nanoparticles. For Cr_2O_3-G NPs synthesized using *Cordyline fruticosa* extract, the spectrum exhibited absorption bands at 1635 cm^{-1} (C=C stretching of alkenes), 1075 cm^{-1} (C–N stretching of amines) [13, 14], and ~870 cm^{-1}, corresponding to the bending vibration of the C=O group in inorganic carbonates [15]. The band at ~625 cm^{-1} is assigned to Cr–O stretching vibrations, consistent with previously reported FTIR spectra of Cr_2O_3 nanoparticles [13–15]. A strong absorption peak at 536 cm^{-1} further confirms the presence of Cr–O and Cr=O vibrational modes, while weaker bands at 481 cm^{-1} and 421 cm^{-1} are attributed to Cr–O bending vibrations [15].

In the case of Cr_2O_3-C NPs, synthesized via the solvent-controlled method using ethanal as a capping agent, the spectrum displayed peaks at 1630 cm^{-1} (C=C stretching of alkenes), 1099 cm^{-1} (C–O stretching), and 880 cm^{-1} (C–H bending) [15], as shown in Fig. 2. Vibrational modes at 612 cm^{-1}, 526 cm^{-1}, and 431 cm^{-1} correspond to Cr–O stretching and bending vibrations [15]. The strong

Table 1 Vibrational modes, corresponding wavenumbers, calculated force constants (k), and bond lengths (R) for Cr_2O_3-G and Cr_2O_3-C nanoparticles

Samples	Bond	Mode	Wavenumber (cm^{-1})	k (Mdynes/cm)	Bond length (Å)
Cr_2O_3-G	Cr-O	stretching vibrations	625	0.2816	2.27
	Cr-O	stretching vibrational	536	0.2073	2.40
	Cr–O	bending vibrations	481	0.1670	2.50
	Cr–O	bending vibrations	421	0.1281	2.63
Cr_2O_3-C	Cr–O	stretching vibrations	612.28	0.2704	2.29
	Cr-O	stretching vibrational	526	0.1999	2.42
	Cr–O	bending vibrations	431	0.1340	2.61

absorption band at 526 cm^{-1} and the relatively weak band at 431 cm^{-1} both indicate the presence of Cr–O bonds [16].

3.1.1 Bond length determination

The Cr–O bond lengths in Cr_2O_3-G and Cr_2O_3-C nanoparticles were calculated from the vibrational frequencies obtained from the FTIR spectra. The relation between vibrational frequency, force constant (k), and bond length (R) is [17]:

$$R = \sqrt{[3]}\frac{C_{ij}}{k} + D_{ij} \tag{2}$$

where C_{ij} and D_{ij} are empirical fitting constants determined by the periodic table period of the bonded atoms. For Cr–O, $D_{ij} = 1.06$ Å and $C_{ij} = 0.5$ [18]. The force constant (k) was calculated from the vibrational frequency using:

$$v = \frac{1}{2\pi c}\sqrt{\frac{k}{\mu}} \tag{3}$$

Here, μ is the reduced mass of the bonded atoms, given by:

$$\mu = \frac{m_1 . m_2}{m_1 + m_2} \tag{4}$$

where m_1 and m_2 are the atomic masses of the bonded atoms. Rearranging Eq. (3) yields the expression for k:

$$k = 4\pi^2 c^2 v^2 \mu \tag{5}$$

The specific wavenumbers corresponding to each vibrational mode were analyzed, and the calculated results are summarized in Table 1. For Cr_2O_3-G nanoparticles, stretching vibrations at 625 cm^{-1} and 536 cm^{-1} corresponded to bond lengths of 2.27 Å and 2.40 Å, respectively, while bending modes at 481 cm^{-1} and 421 cm^{-1} yielded longer bond lengths of 2.50 Å and 2.63 Å. For Cr_2O_3-C nanoparticles, stretching vibrations at 612 cm^{-1} and 526 cm^{-1} gave bond lengths of 2.29 Å and 2.42 Å, while the bending mode at 431 cm^{-1} corresponded to 2.61 Å. These findings indicate that stretching vibrations are associated with shorter, stronger Cr–O bonds, whereas bending vibrations correspond to relatively longer and weaker bonds.

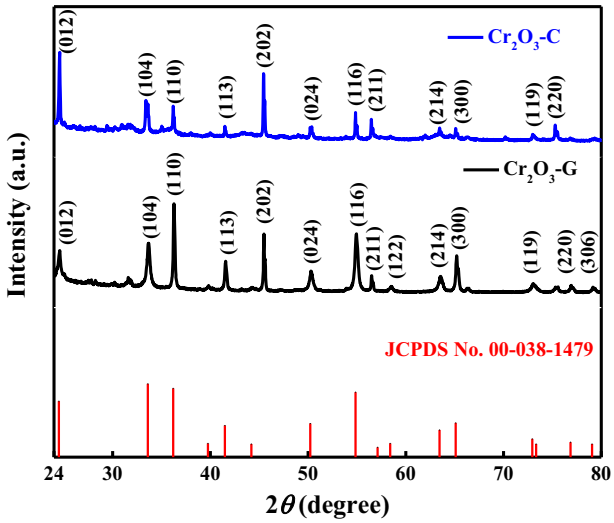


Fig. 3 XRD patterns of Cr2O3 NPs synthesized via green and sol-gel methods

3.2 Structure analysis

The XRD patterns of Cr_2O_3-G and Cr_2O_3-C nanoparticles are presented in Fig. 3. Both samples exhibit sharp and intense diffraction peaks, confirming their polycrystalline nature. For Cr_2O_3-C, the diffraction peaks appear at 2θ values of 24.5°, 33.2°, 36.2°, 41.5°, 44.2°, 50.6°, 54.8°, 57.1°, 63.2°, 65.6°, 73.3°, and 76.6°, corresponding to the (012), (104), (110), (113), (202), (024), (116), (211), (214), (300), (119), and (220) planes, respectively. In contrast, Cr_2O_3-G shows additional reflections at 58.3° and 78.3°, giving a total of fourteen peaks at 2θ values of 24.5°, 33.4°, 36.2°, 41.5°, 44.3°, 51.6°, 54.9°, 57.1°, 58.3°, 63.4°, 65.7°, 73.3°, 77.1°, and 78.3°, which can be indexed to the planes (012), (104), (110), (113), (202), (024), (116), (211), (122), (214), (300), (119), (220), and (306), respectively. All diffraction peaks for both samples are consistent with the rhombohedral structure of Cr_2O_3 (JCPDS card no. 00-038-1479), indicating the absence of secondary phases.

The additional reflections observed in Cr_2O_3-G arise from higher relative intensities of certain planes (e.g., (122), (214), (306), and (220)), which are less distinguishable in Cr_2O_3-C due to peak broadening and reduced intensity. This difference is attributed to variations in crystallite size and crystallinity between the two samples rather than a change in crystal phase.

The interplanar spacings (d) were calculated from Bragg's law,

$$n\lambda = 2dsin\theta$$

and the lattice constants were refined using the hexagonal form of the rhombohedral relation:

$$\frac{1}{d^2} = \frac{4}{3}\frac{h^2 + hk + k^2}{a^2} + \frac{l^2}{c^2}$$

Least-squares refinement of the observed *d*-values yielded lattice constants of $a = 4.957$ Å, $c = 13.611$ Å for Cr_2O_3-C, and $a = 4.950$ Å, $c = 13.643$ Å for Cr_2O_3-G, in excellent agreement with reference values. The slight differences in lattice constants between the two samples indicate subtle variations in crystallinity, likely arising from the synthesis method. In particular, the appearance of additional reflections in Cr_2O_3-G (e.g., (122), (214), (306), and (220)) suggests enhanced crystallinity compared to Cr_2O_3-C, where peak broadening reduces their visibility [19].

Bond lengths were estimated using the refined lattice parameters together with the standard atomic positional parameters for corundum-type Cr_2O_3 (Cr at (0,0,z) with z ≈ 0.352, O at (x,0,¼) with x ≈ 0.306). The calculated Cr–O bond lengths split into two sets, as expected for the distorted octahedral coordination of Cr^{3+}, giving values of approximately 1.97 Å for the shorter bonds (three per Cr atom) and 2.02 Å for the longer bonds (three per Cr atom). Thus, each Cr atom is octahedrally coordinated by six oxygen atoms, consistent with the corundum structure. The observed bond lengths and lattice parameters confirm that both Cr_2O_3-C and Cr_2O_3-G retain the rhombohedral crystal phase [20], and that the structural differences between the samples are attributable to variations in crystallite size and crystallinity rather than a change in crystal symmetry.

When compared with the FTIR-derived bond lengths, a notable difference is observed. FTIR analysis revealed stretching modes corresponding to Cr–O bonds of 2.27–2.42 Å, and bending modes corresponding to longer Cr–O bonds of 2.50–2.63 Å (Table 1). This difference arises from the distinct principles of the two techniques: XRD provides the static, average crystallographic bond distances in the bulk lattice, while FTIR evaluates dynamic bond lengths associated with vibrational states. Vibrational methods often yield slightly longer effective bond distances due to anharmonicity and contributions from weaker bending modes. Thus, while both methods confirm the octahedral coordination of Cr^{3+}, the XRD bond lengths (1.97–2.02 Å) represent the precise crystallographic geometry, whereas the FTIR bond lengths (2.27–2.63 Å) reflect the vibrational dynamics of Cr–O bonds. The complementary agreement between these methods strengthens the structural analysis of Cr_2O_3 nanoparticles.

The crystallite sizes (*D*) of the nanoparticles were determined using the Scherrer equation as in Eq. (6) [19]:

$$D = \frac{K\lambda}{\beta\cos\theta} \tag{6}$$

where *D* represents the crystallite size, λ is the X-ray wavelength (0.15406 nm), *K* is the Scherrer constant (0.9), β is the full width at half maximum (FWHM) in radians, and θ is the Bragg angle of diffraction in radians. For the green-synthesized Cr_2O_3 NPs, the calculated crystallite size at the given 2θ values was 38 nm, whereas for the chemically synthesized Cr_2O_3 NPs, the size was 44 nm.

3.2.1 Williamson Hall (W-H) model

The Scherrer equation primarily considers the effect of crystallite size on XRD peak broadening, while neglecting contributions from other lattice microstructures such as intrinsic strain due to defects in nanocrystals, grain boundaries, and stacking faults. In contrast, the Williamson-Hall (W-H) method accounts for both crystallite size (*D*) and intrinsic lattice strain (ε), making it a more accurate and preferred technique [19, 21–23]. The equation is given as:

$$\beta\cos\theta = \frac{k\lambda}{D} + 4\varepsilon\sin\theta \tag{7}$$

To estimate D and ε, a graph was plotted with $\beta\cos\theta$ on the y-axis and $4\sin\theta$ on the x-axis, as shown in Fig. 4. The slope and intercept of the fitted straight line correspond to ε and D, respectively. The goodness of fit was evaluated, and the coefficient of determination (R^2) was found to be greater than 0.55 for both Cr_2O_3-G and Cr_2O_3-C, confirming a reasonable correlation for the W-H analysis. The D and ε are listed in Table 2. The *D* values obtained for Cr_2O_3-G and Cr_2O_3-C are 48 nm and 58 nm, respectively, while the ε values are 0.0061 and 0.0121 for Cr_2O_3-G and Cr_2O_3-C nanoparticles.

The structural properties of nanoparticles can be further analyzed through key parameters such as X-ray density (ρ), specific surface area (SSA), and dislocation density (δ). The X-ray density (ρ) is calculated using Eq. (8) [23]:

$$\rho = \frac{Z.M}{N_A \cdot V_c} \tag{8}$$

where Z is the number of formula units per unit cell (6 for Cr_2O_3), M is the molar mass (152.00 g/mol), N_A is Avogadro's number (6.022×10^{23} mol^{-1}), and V_c is the unit cell volume.

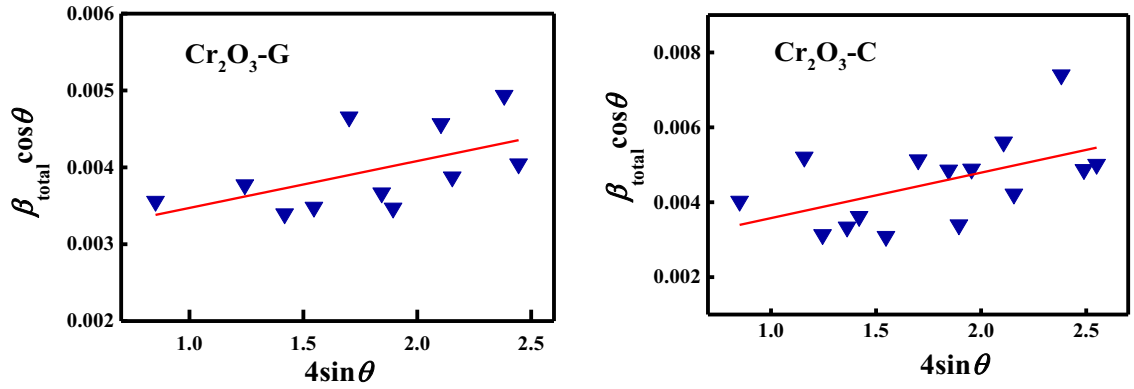


Fig. 4 Williamson-Hall (W–H) plot for Cr_2O_3 NPs synthesized via green and sol-gel methods

This gives an X-ray density of approximately 5.22 g/cm³. The specific surface area (SSA) was determined using the crystallite size (D) and X-ray density (ρ) as in Eq. (9) [23]:

$$SSA = \frac{6}{D.\rho} \tag{9}$$

The SSA values calculated from both methods are presented in Table 2. The SSA was found to be 30 m²/g and 26 m²/g for Cr_2O_3-G and Cr_2O_3-C, respectively, using the D obtained from the Scherrer equation. Using the D values obtained from the W-H method, the SSA values were 24 m²/g and 20 m²/g. The Cr_2O_3-G nanoparticles have a larger specific surface area, which enhances their photocatalytic properties due to their smaller particle size and improved morphology.

Dislocation density (δ) as shown in Eq. (10) is a parameter used to estimate the number of defects in Cr_2O_3 samples, representing the length of dislocation lines per unit volume [24]:

$$\delta = \frac{1}{D^2} \tag{10}$$

The dislocation density (ρ in 10^{14}, lines/m^2) for the Scherrer Method and W-H Method is as follows: the Cr_2O_3-G has a dislocation density of 6.92 lines/m^2 for the Scherrer Method and 4.34 lines/m^2 for the W-H Method, while the chemically synthesized Cr_2O_3-C shows values of 5.16 and 2.97 lines/m^2, respectively. These relatively low dislocation density values indicate that both samples exhibit a high degree of crystallinity. However, the higher dislocation density in Cr_2O_3-G suggests a slightly lower crystal quality compared to Cr_2O_3-C, though both samples still demonstrate good crystallinity.

3.3 Optical properties

The optical band gap (E_g) of the synthesized nanoparticles was determined from UV–Vis absorption spectra. For the measurements, the samples were first sonicated in deionized water, and their absorption spectra were recorded, as shown Fig. 5. Two distinct absorption maxima were observed at 272 nm and 371 nm for both Cr_2O_3-G and Cr_2O_3-C nanoparticles. These peaks correspond to the electronic transitions $^4A_2g \rightarrow {}^4T_1g$ and $^4A_2g \rightarrow {}^4T_2g$ of Cr^{3+} ions in octahedral coordination [25–27].

The optical band gap was evaluated using the Tauc relation (Eq. 11) [28]:

$$\alpha h\nu = k(h\nu - E_g)^{\frac{1}{n}} \tag{11}$$

where α is the absorption coefficient, $h\nu$ is the photon energy, n depends on the type of electronic transition (with $n = 2$ used here for direct transitions), and k is the transition probability. The absorption coefficient α was calculated using the following equation [21]:

$$\alpha = 2.303 \times \frac{1000\rho A}{lCM} \tag{12}$$

where ρ is the density, A is the absorbance, l is the optical path length (1 cm), C is the molar concentration, and M is the molar mass.

Figure 6 presents the Tauc plots of $(\alpha h\nu)^2$ versus hν for each sample. The linear portions near the absorption edges were extrapolated to intersect the hν-axis at $(\alpha h\nu)^2 = 0$, corresponding to the E_g values. Two distinct band gaps were obtained for both materials: 3.05 and 4.15 eV for Cr_2O_3-G, and 3.07 and 4.17 eV for Cr_2O_3-C (Table 2). The results indicate that both samples exhibit nearly identical optical properties, with minor variations likely arising from differences in synthesis conditions. A similar two-band absorption feature has previously been reported for nanostructured TiO_2 thin films deposited on Cu mesh [29].

The observation of two optical band gaps in our Cr_2O_3 nanoparticles can be attributed to several factors. First, particle size and surface states play a crucial role in

Table 2 Structural and optical properties of Cr_2O_3-G (green synthesis) and Cr_2O_3-C (sol-gel synthesis) nanoparticles

Samples	Bandgap (eV)		Crystalline size (nm)		Lattice Strain ($\times 10^{-3}$)	Specific Surface Area (m^2/g)		Dislocation Density (lines/m^2) ($\times 10^{14}$)		PSA (nm)	Zeta Potential (mV)
	$^4A_2g \rightarrow {}^4T_1g$	$^4A_2g \rightarrow {}^4T_2g$	Scherrer Method	(W-H) method	(W-H) method	Scherrer Method	(W-H) method	Scherrer Method	(W-H) method		
Cr_2O_3-G	3.05	4.15	38	48	0.6101	30	24	6.92	4.34	143	-44.3
Cr_2O_3-C	3.07	4.17	44	58	1.21	26	20	5.16	2.97	207	-21.5

Band gaps correspond to the $^4A_2g \rightarrow {}^4T_1g$ and $^4A_2g \rightarrow {}^4T_2g$ transitions of Cr^{3+} ions; crystallite size, strain, surface area, and dislocation density were derived from XRD, while PSA and zeta potential reflect dispersion stability.

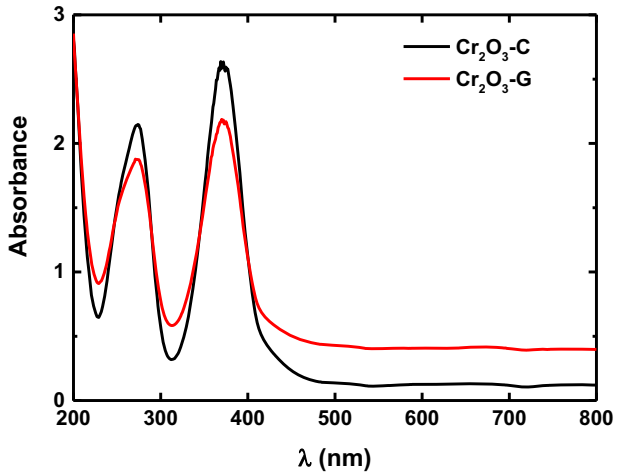


Fig. 5 UV absorbance spectra of Cr_2O_3 NPs synthesized by green and sol–gel methods

determining the electronic structure. A reduction in particle size can induce quantum confinement, leading to band gap widening relative to bulk Cr_2O_3 (~3.2–3.4 eV) [26, 30]. The higher-energy gap (~4.15–4.17 eV) observed in this work agrees with earlier reports of size-dependent blue shifts in Cr_2O_3 nanoparticles (up to ~4.3 eV) [26]. Additionally, surface defects and oxygen vacancies may introduce localized electronic states, thereby producing multiple absorption edges [30]. Second, mixed oxidation states of chromium ions can further contribute to the dual-gap behavior. While the transitions at 272 and 371 nm are associated with Cr^{3+} ions ($^4A_2g \rightarrow {}^4T_1g$ and $^4A_2g \rightarrow {}^4T_2g$) [25–27], the presence of Cr^{4+} ions has been linked to higher-energy charge-transfer transitions [26].

Compared with bulk Cr_2O_3, the band gaps obtained here show a clear blue shift, confirming the combined influence of size confinement and defect-related states. The two-band absorption pattern observed in our samples is consistent with previously reports [25–27]. From an application perspective, the dual band gap structure may be beneficial for photocatalysis. The lower-energy gap (~3.05–3.07 eV) enables visible-light absorption, while the higher-energy gap (~4.15–4.17 eV) extends activity into the UV region. Together, these features enhance light-harvesting efficiency and promote effective electron–hole pair generation, which are advantageous for improving photocatalytic performance.

3.4 Particle size and zeta potential analysis

Dynamic light scattering (DLS) was employed to determine the hydrodynamic particle sizes of the Cr_2O_3 nanoparticles. As shown in Fig. 7a, the average diameters were 143 nm for Cr_2O_3-G and 207 nm for Cr_2O_3-C (Table 2). Although these values exceed 100 nm, it is important to note that DLS measures the *hydrodynamic diameter*, which includes the solvation layer and possible agglomeration of particles in suspension, often resulting in larger apparent sizes. In contrast, XRD analysis confirmed that the crystallite sizes are 38–44 nm (Scherrer method) and 48–58 nm (Williamson–Hall method), well within the nanoscale range. Thus, despite the larger hydrodynamic sizes, the true crystalline domains of Cr_2O_3 remain nanosized, consistent with previous reports for nanoparticle systems [21, 23].

To further assess colloidal stability, zeta potential (ZP) analysis was performed (Fig. 7b). A ZP threshold of ±30 mV is generally used to distinguish stable from unstable suspensions, where values above this threshold indicate sufficient electrostatic repulsion to prevent aggregation [23]. The Cr_2O_3-G nanoparticles exhibited a ZP of −44.3 mV, confirming excellent dispersion stability, while Cr_2O_3-C showed a lower ZP of −21.5 mV (Table 2), suggesting a higher tendency for aggregation. The higher negative surface charge of Cr_2O_3-G not only suppresses clustering but also increases effective surface area and promotes stronger interactions with dye molecules, which can enhance photocatalytic activity [31].

3.5 Scanning electron microscopy and energy dispersive X-ray

Morphological analysis was conducted using SEM combined with EDX analysis. The SEM images reveal a porous structure with agglomerated particles, as shown in Fig. 8. The Cr_2O_3-G NPs exhibit a hexagonal morphology, while the Cr_2O_3-C NPs display a cubic morphology.

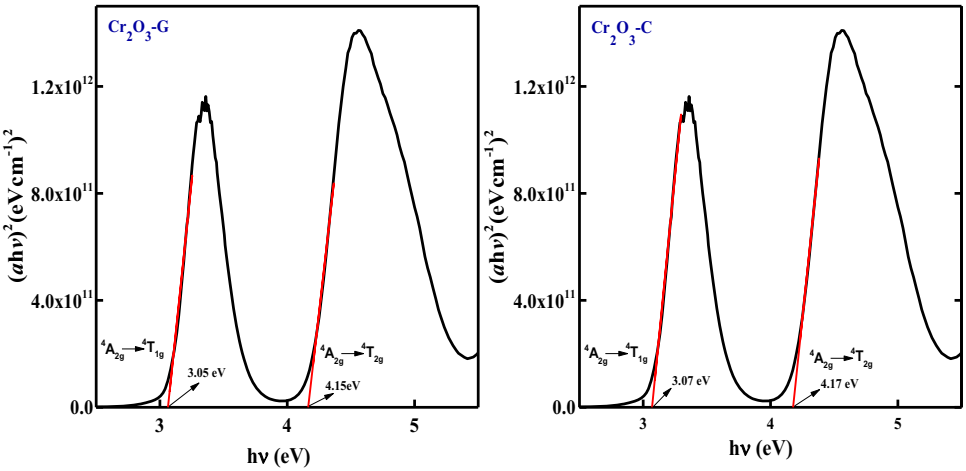


Fig. 6 UV absorbance spectra (inset) and Tauc plots of Cr_2O_3 NPs synthesized by green and sol–gel methods

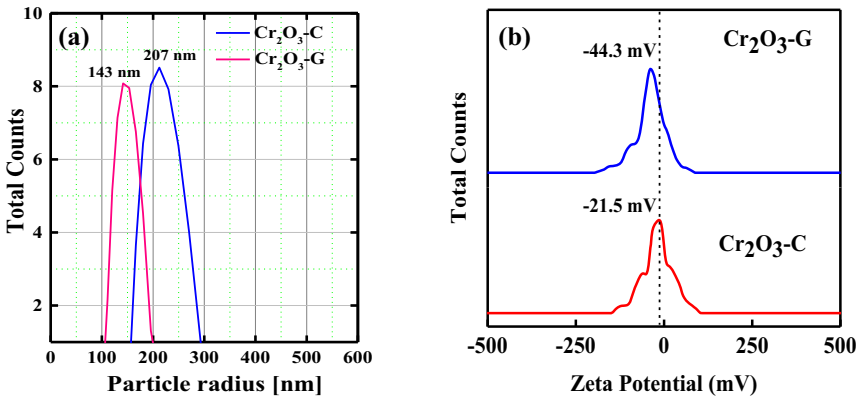


Fig. 7 **a** Dynamic light scattering (DLS) and **b** zeta potential analysis of Cr_2O_3 nanoparticles synthesized via green (Cr_2O_3-G) and sol–gel (Cr_2O_3-C) methods

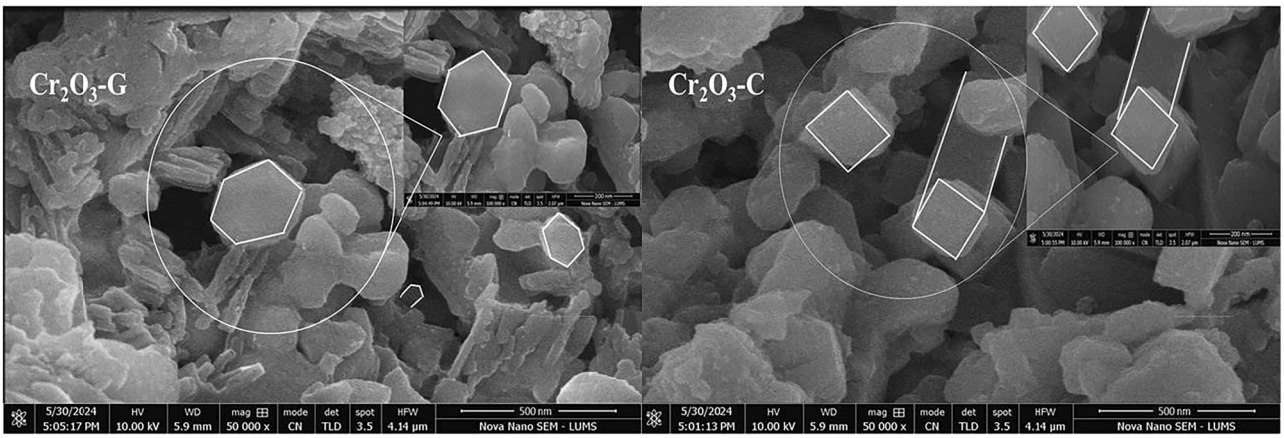


Fig. 8 SEM images of Cr_2O_3-G and Cr_2O_3-C nanoparticles showing porous and agglomerated structures

A comparison of the SEM images indicates that Cr_2O_3-G NPs are smaller than Cr_2O_3-C NPs, resulting in a higher surface-to-volume ratio, which enhances their effectiveness for MB dye photodegradation.

The elemental composition of the sample was determined using EDX. The EDX spectra of Cr_2O_3-G NPs and Cr_2O_3-C NPs confirmed that the nanoparticles predominantly consisted of chromium and oxygen, as shown in Fig. 9. The experimental weight percentages of chromium and oxygen were 65.3% and 30.4%, respectively, for Cr_2O_3-G NPs, and 64.0% and 30.3% for Cr_2O_3-C NPs, closely matching the theoretical values of 68.4% for chromium and 31.6% for oxygen. Additionally, the EDX spectrum revealed a prominent peak for chloride, which is likely attributed to adsorbed salt on the surface of the Cr_2O_3 NPs [32].

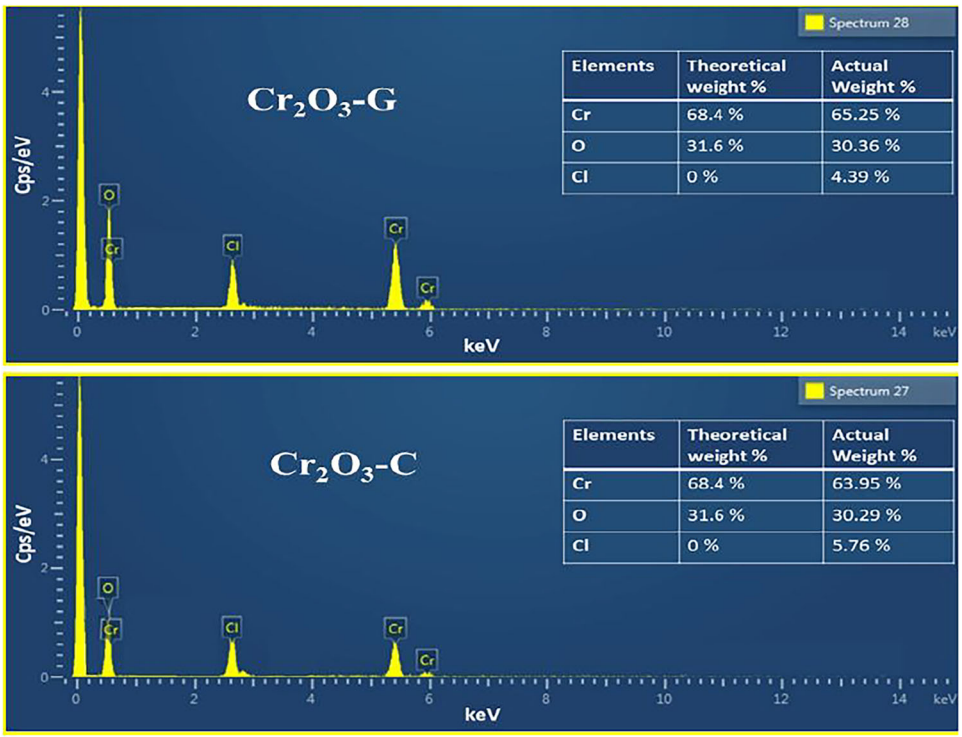


Fig. 9 EDX spectra of Cr_2O_3-G and Cr_2O_3-C nanoparticles confirming the elemental composition

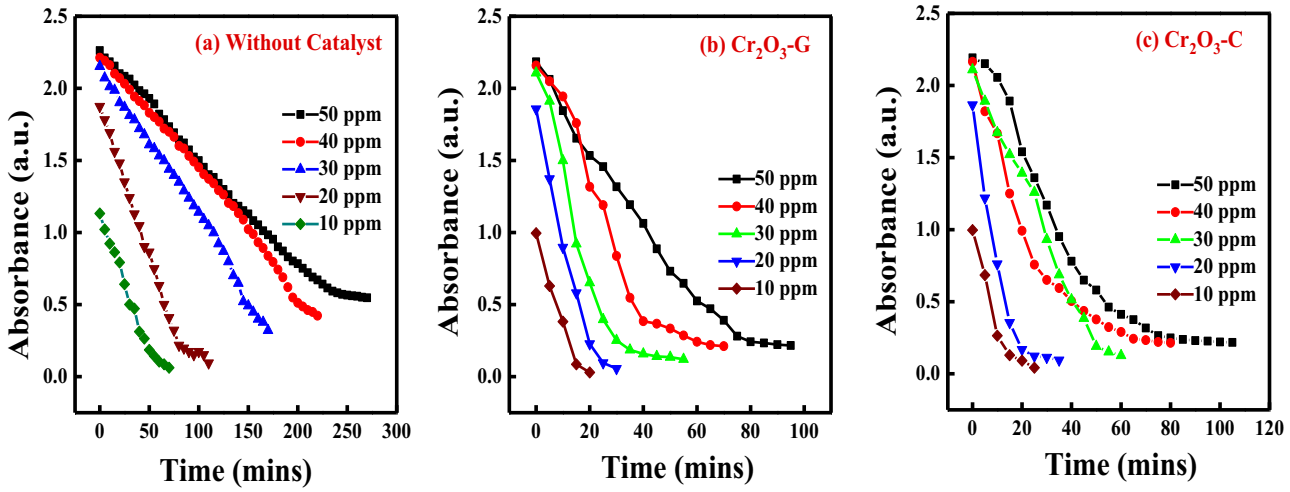


Fig. 10 Absorbance of MB for **a** without catalyst, **b** Cr_2O_3-G NPs synthesized using Cordyline fruticosa, and **c** Cr_2O_3-C NPs prepared via the sol-gel method with ethanol as a capping agent

3.6 Photocatalytic degradation of methylene blue

3.6.1 Kinetics of degradation process

The degradation of MB at varying concentrations (10–50 ppm) was investigated using a fixed catalyst dosage of 0.02 g under tubular UV irradiation. The maximum absorption wavelength of MB (664 nm) remained unchanged, and absorbance was recorded every 5 minutes (Fig. 10). A steady decline in absorbance confirmed progressive dye degradation.

Reaction kinetics were analyzed using the Langmuir–Hinshelwood model (Eq. 13) [4, 5, 28, 33]:

$$ln\left(\frac{A_0}{A_t}\right) = -kt \tag{13}$$

where A_0 and A_t represent the initial and time-dependent dye concentrations, and k is the rate constant. Linear plots of

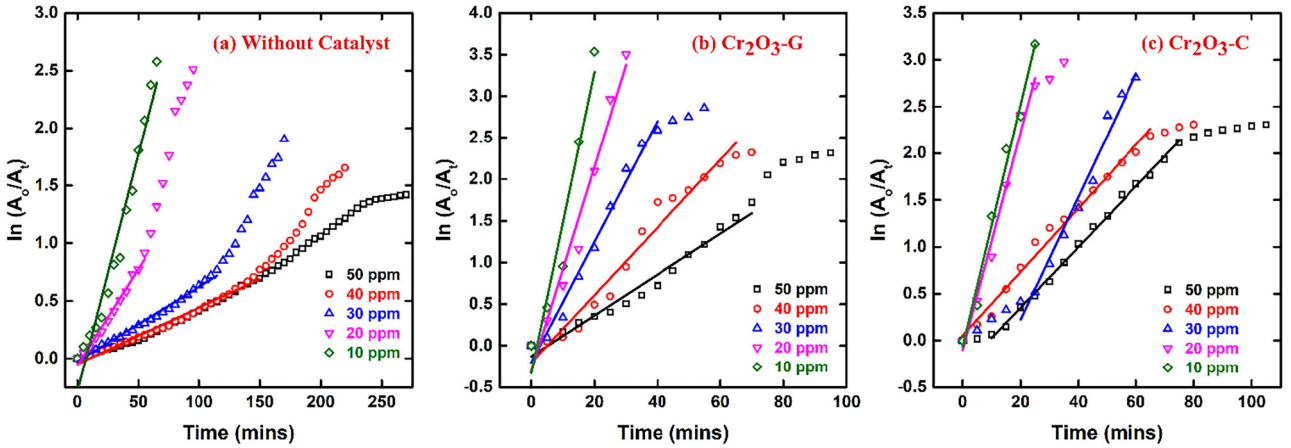


Fig. 11 Pseudo-first-order kinetics of MB degradation for **a** without catalyst, **b** Cr_2O_3-G NPs synthesized using Cordyline fruticosa, and **c** Cr_2O_3-C NPs prepared through the sol-gel method with ethanol as a capping agent

Table 3 Photocatalytic degradation of MB by Cr_2O_3-G (green) and Cr_2O_3-C (sol–gel) nanoparticles at different concentrations (0.02 g catalyst), showing % degradation and kinetic parameters

MB Conc. (ppm)	Without Catalyst				Cr_2O_3-C				Cr_2O_3-G			
	Time (min)	%D	k (min^{-1})	R^2	Time (min)	%D	k (min^{-1})	R^2	Time (min)	%D	k (min^{-1})	R^2
10	70	94	0.04122	0.983	25	96	0.12918	0.983	20	97	0.18121	0.973
20	115	92	0.01672	0.984	35	95	0.11625	0.983	30	96	0.12281	0.964
30	170	85	0.00646	0.989	60	94	0.06556	0.974	55	94	0.07254	0.981
40	220	81	0.00491	0.985	80	91	0.03393	0.989	70	92	0.04058	0.964
50	270	76	0.00568	0.959	100	90	0.03235	0.996	95	91	0.02455	0.973

$\ln\left(\frac{A_0}{A_t}\right)$ versus irradiation time (t) (Fig. 11) showed excellent fits ($R^2 > 0.96$), confirming pseudo-first-order kinetics. The calculated slope (k) and R^2 values are summarized in Table 3.

3.6.2 Effect of irradiation time

Figure 12 illustrates MB degradation over different irradiation times. Without catalyst, degradation was slow, requiring 270 minutes for 50 ppm and 70 minutes for 10 ppm. In contrast, Cr_2O_3-C shortened degradation times to 100 minutes (50 ppm) and 25 minutes (10 ppm). Cr_2O_3-G showed even higher activity, achieving 97% degradation at 10 ppm in 20 minutes and 91% at 50 ppm in 95 minutes. The enhanced efficiency of Cr_2O_3-G is attributed to its smaller particle size and higher surface area, providing more active sites for photocatalysis.

3.6.3 Effect of concentration

The initial dye concentration significantly affected photocatalytic efficiency (Fig. 13). At 10 ppm, Cr_2O_3-G achieved 97% degradation, slightly higher than Cr_2O_3-C (96%). At 50 ppm, efficiencies declined modestly to 91% (Cr_2O_3-G) and 90% (Cr_2O_3-C), while only 76% degradation was observed without a catalyst. The superior performance of Cr_2O_3-G arises from its lower bandgap energy (3.05 eV) and smaller crystallite size, which enhance light absorption, electron–hole pair separation, and catalytic activity, particularly at higher dye concentrations.

3.6.4 Effect of contact time on methylene blue degradation with Cr_2O_3 NPs

Contact time also played a critical role (Fig. 14). At 50 ppm without catalyst, 75% degradation required 270 minutes. In contrast, Cr_2O_3-C achieved 88% degradation in 100 minutes, while Cr_2O_3-G reached 89% in 95 minutes. At 10 ppm, Cr_2O_3-G achieved 97% degradation in only 20 minutes compared to 25 minutes for Cr_2O_3-C. These results demonstrate the superior photocatalytic activity of Cr_2O_3-G, attributed to its smaller particle size (48 nm), higher surface area, and reduced bandgap, which collectively enhance light absorption and charge carrier dynamics. Both catalysts were easily recovered after reaction, confirming their reusability.

To benchmark performance, results from the present study were compared with literature reports (Table 4). Conventional Cr_2O_3 catalysts generally require higher dosages and longer irradiation times to achieve only

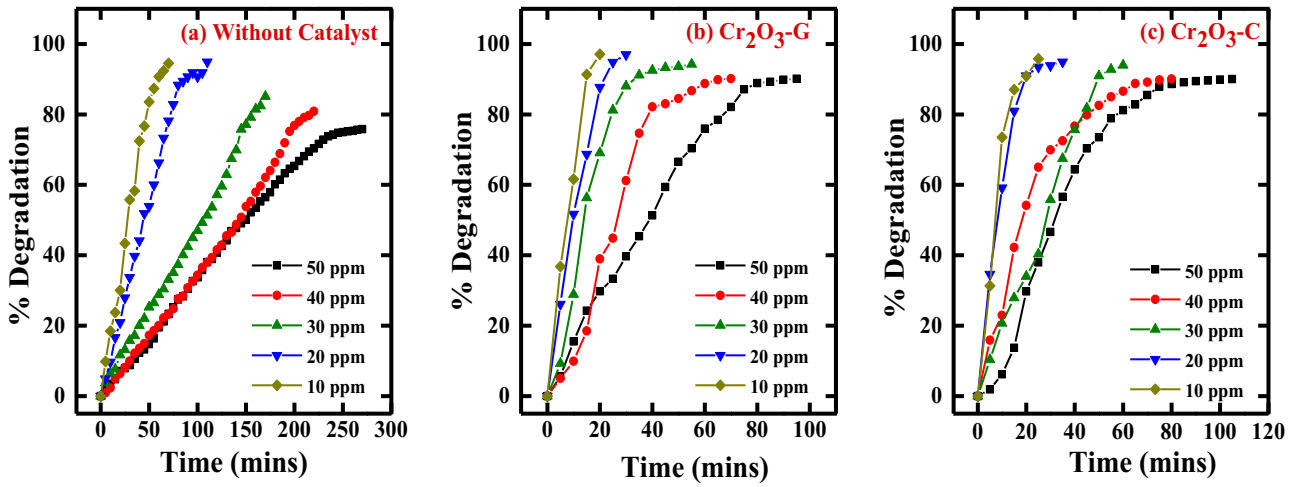


Fig. 12 Percentage degradation of MB under irradiation: **a** without catalyst, **b** Cr_2O_3-G NPs synthesized using *Cordyline fruticosa*, and **c** Cr_2O_3-C NPs prepared via the sol–gel method

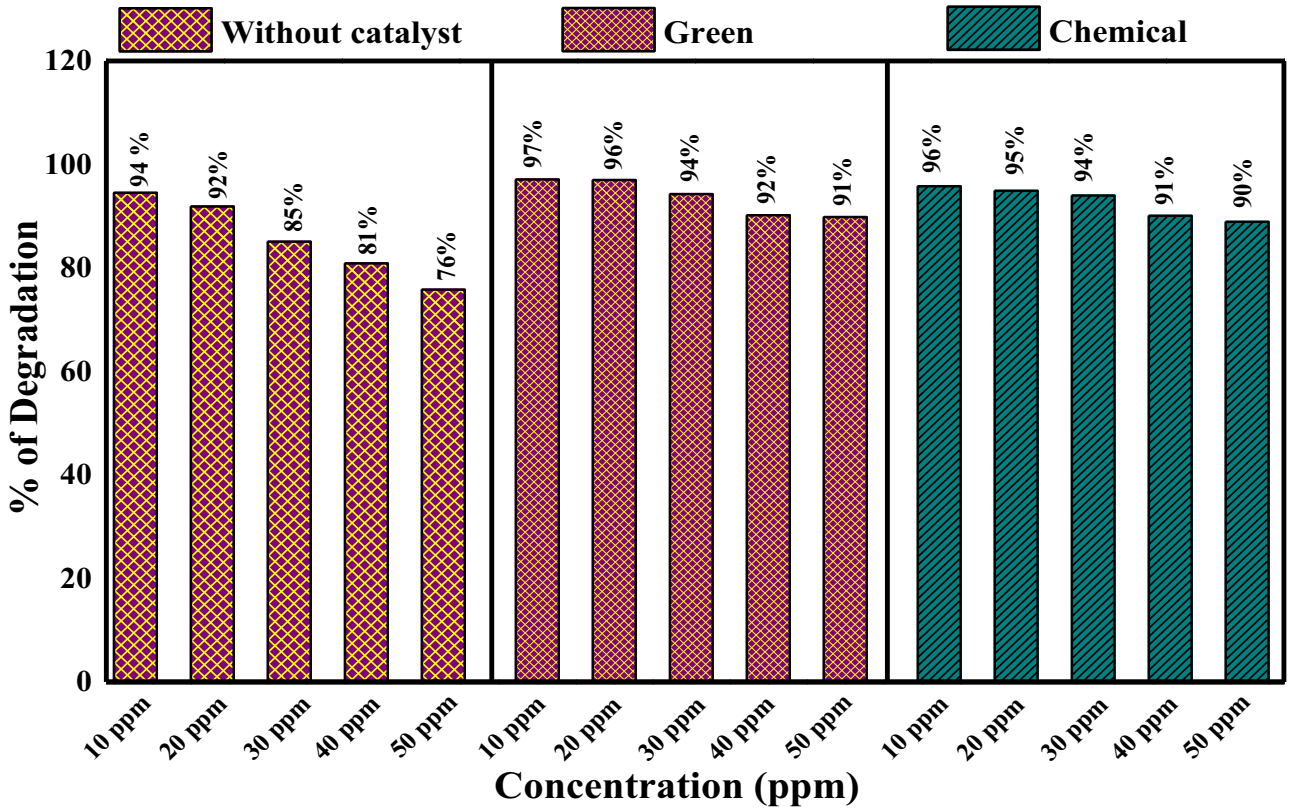


Fig. 13 Photocatalytic degradation of MB at different initial concentrations using Cr_2O_3-G, Cr_2O_3-C, and without catalyst

moderate degradation, whereas Cr_2O_3-G and Cr_2O_3-C reached up to 96% degradation with shorter irradiation times and lower catalyst loadings. This highlights the effectiveness of the green synthesis route in enhancing photocatalytic efficiency.

The superior photocatalytic efficiency of Cr_2O_3-G can be directly attributed to its structural, optical, and morphological features. XRD analysis revealed that Cr_2O_3-G possessed smaller crystallite sizes than Cr_2O_3-C, which increases surface-to-volume ratio and provides more active sites for dye adsorption and degradation. Optical studies showed that Cr_2O_3-G exhibited a slightly narrower band gap (3.05 eV) than Cr_2O_3-C (3.07 eV), enabling improved visible-light absorption and more efficient electron–hole pair

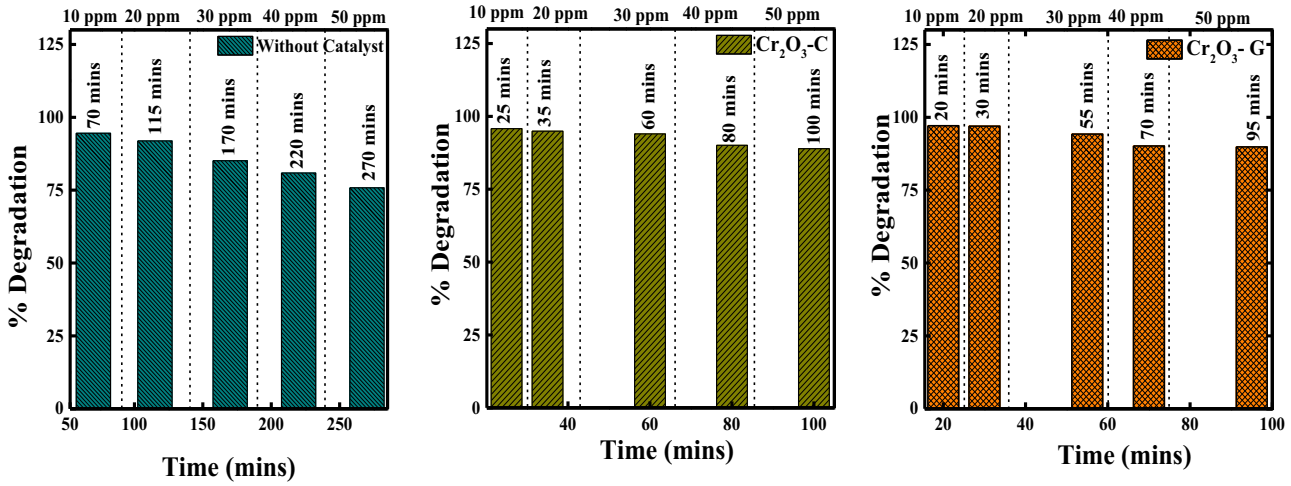


Fig. 14 Percentage degradation of MB at different contact times using Cr_2O_3-G, Cr_2O_3-C, and without catalyst

Table 4 Comparison of photocatalytic degradation efficiency of methylene blue using Cr_2O_3-based nanoparticles synthesized by different methods, highlighting catalyst dosage, degradation performance, and synthesis approach

Material	Conc. (ppm)	Time (min)	Degradation (%)	Dosage (g/L)	Method	References
Cr_2O_3	10	240	30	0.1	Chemical	[37]
Cr_2O_3	10	100	99	0.0005	Green	[38]
Cr_2O_3	20	130	26	0.01	Green	[39]
Cr_2O_3	10	180	85	0.01	Green	[40]
NiO/Cr_2O_3	10	180	93	0.005	Chemical reduction	[41]
$Ag–Cr_2O_3$	10	100	96	0.015	Chemical	[3]
Cr_2O_3/Bi_2S_3	–	400	90	0.5	Hydrothermal	[42]
Cr_2O_3-G	20/30/40	30/55/70	96/94/90	0.02	Green (Present work)	-
Cr_2O_3-C	20/30/40	35/60/80	95/93/90	0.02	Sol–gel (Present work)	-

generation. Furthermore, DLS and zeta potential results confirmed higher colloidal stability for Cr_2O_3-G (−44.3 mV) compared to Cr_2O_3-C (−21.5 mV), reducing agglomeration and ensuring better dispersion in aqueous solution. SEM images further demonstrated that Cr_2O_3-G formed more uniform and finer particles, while EDX confirmed high purity in both samples. Collectively, these structural and optical advantages explain the enhanced photocatalytic activity of Cr_2O_3-G, which achieved faster and higher methylene blue degradation compared to Cr_2O_3-C.

3.7 Photodegradation mechanism of Methylene Blue

Photocatalytic degradation experiments were carried out using varying concentrations of MB solutions (10, 20, 30, 40, and 50 ppm), while maintaining a constant catalyst dosage of 0.02 g, as illustrated in Fig. 15. Under UV irradiation, electrons in the valence band are excited, creating holes and forming electron-hole pairs. This charge separation at the catalyst surface triggers the movement of charges, which actively participate in redox reactions. Furthermore, water (H_2O) decomposition can generate highly reactive hydroxyl radicals (•OH). The presence of electrons (e^-) plays a crucial role in the reduction of oxygen (O_2), leading to the formation of hydrogen peroxide (H_2O_2) and superoxide anions (O_2^-) through protonation. These intermediates, in turn, produce additional active hydroxyl radicals [4, 5, 21]. The primary degradation reactions involved in this process are as follows:

$$Cr_2O_3 + h\nu \rightarrow Cr_2O_3(e^-CB) + Cr_2O_3(h^+VB)$$

$$Cr_2O_3(h^+VB) + H_2O \rightarrow Cr_2O_3 + H^+ + HO$$

$$Cr_2O_3(e^-CB) + O_2 \rightarrow Cr_2O_3 + H^+ + O_2^-$$

$$O_2^- + H^+ \rightarrow HOO$$

$$O_2^- + e^-CB + H_2O \rightarrow HOO + OH^-$$

$$HOO + H^+ + e^-CB \rightarrow H_2O_2$$

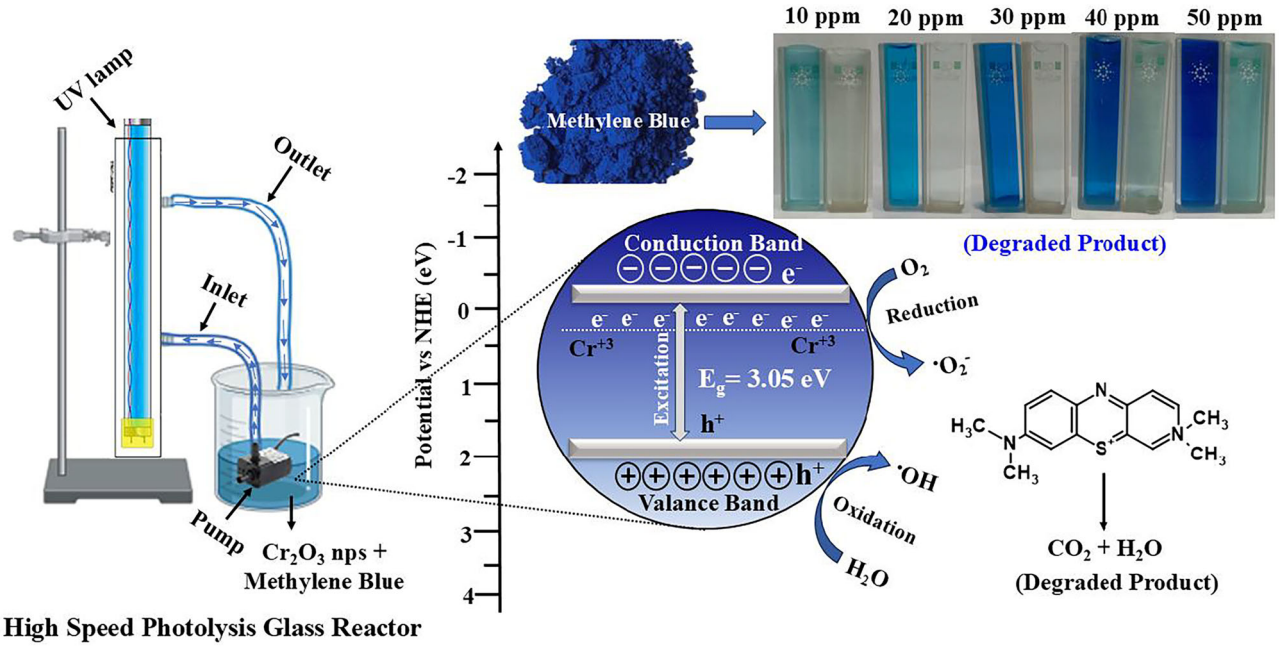


Fig. 15 Photocatalytic degradation mechanism of methylene blue

$$H_2O_2 \rightarrow 2OH$$

$$H_2O + h^+ \rightarrow OH + H^+$$

$$MB + OH \rightarrow CO_2 + H_2O(\text{degradation process})$$

3.7.1 Degradation pathway of methylene blue

The degradation of MB proceeds through a series of complex chemical reactions, as illustrated in Fig. 16, ultimately breaking down the dye into simple molecules such as CO_2, H_2O, NO_3^-, and SO_4^{2-}. The process begins with MB (molecular weight 284 g/mol), which undergoes demethylation to form Azure A (270 g/mol). Successive demethylation produces Azure B (256 g/mol), which then undergoes deamination to yield Safranin (228 g/mol). Safranin is reduced to an amide derivative (164 g/mol), which further decomposes into m-toluidine (122 g/mol) and eventually into aniline (93 g/mol), a simple amine. In an alternative pathway, MB loses its dimethylamino group to form phenothiazine (199 g/mol). Phenothiazine is reduced to thionine (162 g/mol), which subsequently degrades into benzothiazine (149 g/mol). This intermediate is converted into a thiazine derivative (129 g/mol) and finally into 1,4-thiazine (101 g/mol) [2, 34].

A parallel route involves the formation of a phenothiazine derivative (280 g/mol), which undergoes successive transformations into dimethylaminocinnamyl alcohol (147 g/mol), 3-amino-2-methylpent-2-en-1-ol (117 g/mol), and ultimately but-1-en-2-amine (73 g/mol). These pathways involve key chemical processes such as reduction, deamination, and demethylation, reflecting the intricate sequence of reactions responsible for the complete degradation of MB [2, 34, 35].

3.8 Reusability, photostability, and ROS contribution

The long-term stability of photocatalysts is essential for their practical application in large-scale wastewater treatment. The reusability of Cr_2O_3-G and Cr_2O_3-C nanoparticles (NPs) was assessed by monitoring MB degradation at 10, 20, and 30 ppm over three consecutive cycles (Fig. 17). After each run, the catalysts were recovered, dried, and reused.

Cr_2O_3-G NPs retained excellent activity, achieving 94%, 93%, and 91% degradation for 10, 20, and 30 ppm, respectively, after the third cycle. Cr_2O_3-C NPs showed slightly lower but still high efficiencies of 92%, 91%, and 89% under the same conditions (Table 5). Both catalysts demonstrated efficient recyclability, with recovered amounts of 0.017 g (Cr_2O_3-G) and 0.016 g (Cr_2O_3-C) after three cycles.

Structural stability was confirmed by XRD, which showed no changes in the crystallinity of Cr_2O_3-G after repeated use, and by SEM, which revealed that the cubic morphology of Cr_2O_3-C remained intact (Fig. 18). These findings highlight the robust photostability and recyclability of both catalysts.

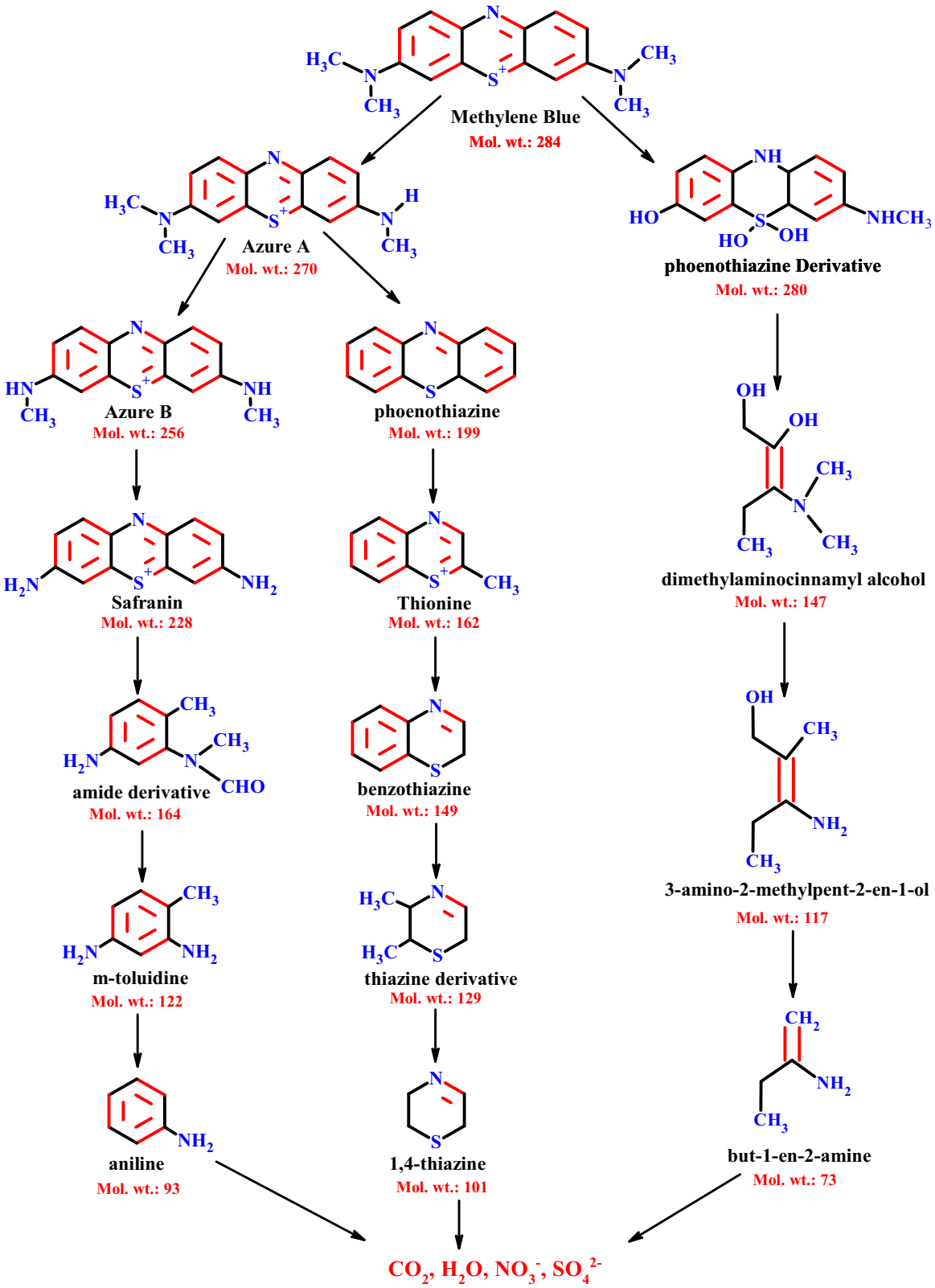


Fig. 16 Proposed pathway for methylene blue degradation

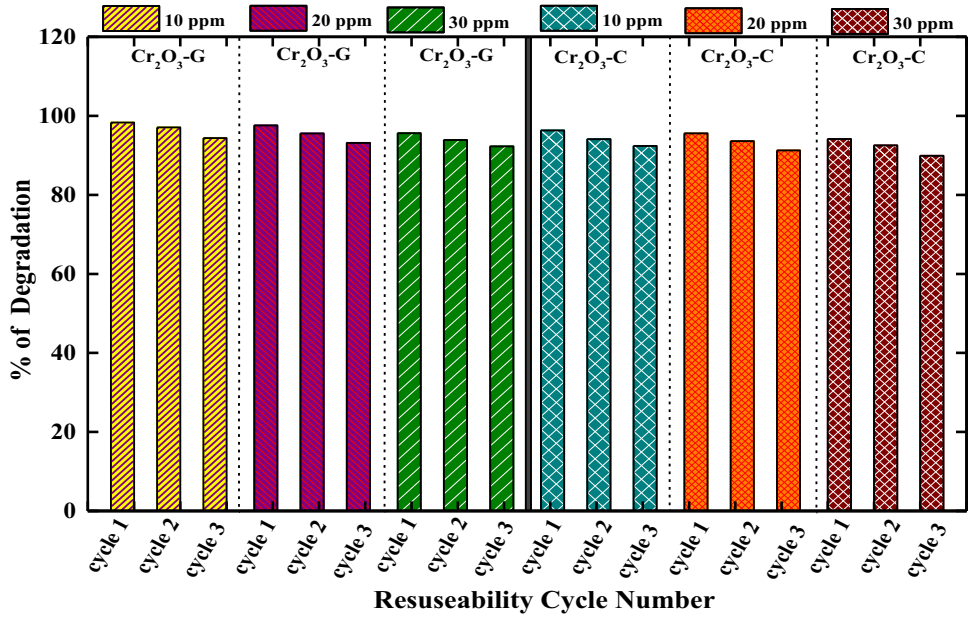


Fig. 17 Reusability and photocatalytic degradation efficiency of Cr_2O_3-G and Cr_2O_3-C nanoparticles at different concentrations

Table 5 Reusability and photocatalytic degradation efficiency of Cr_2O_3-G and Cr_2O_3-C nanoparticles at different MB concentrations (10, 20, and 30 ppm) over three consecutive cycles

Concentration (ppm)	Cr_2O_3-G			Cr_2O_3-C		
	1st Cycle	2nd Cycle	3rd Cycle	1st Cycle	2nd Cycle	3rd Cycle
10	20 min–97%	20 min–95%	20 min–94%	25 min–96%	25 min–94%	25 min–92%
20	30 min–96%	30 min–95%	30 min–93%	35 min–95%	35 min–93%	35 min–91%
30	55 min–94%	55 min–93%	55 min–91%	60 min–94%	60 min–92%	60 min–89%

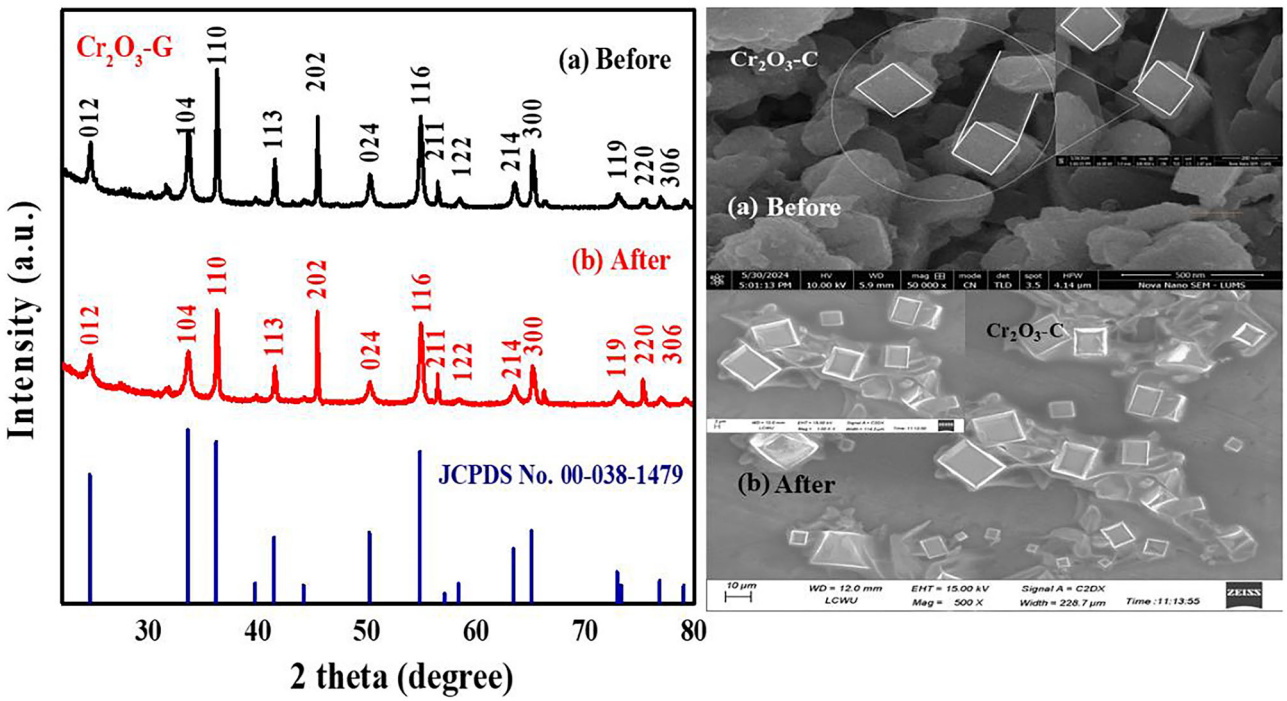


Fig. 18 XRD patterns of Cr_2O_3-G and SEM images of Cr_2O_3-C (**a**) before and **b** after three degradation cycles

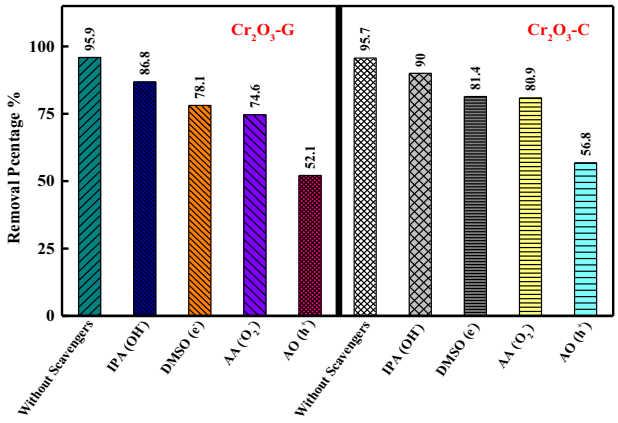


Fig. 19 Scavenger experiments showing the contribution of ROS to MB degradation over Cr_2O_3-G and Cr_2O_3-C, with h^+ as the dominant species, followed by •OH, e^-, and $•O_2^-$

To probe the role of reactive oxygen species (ROS) in MB degradation, scavenger experiments were conducted. In the absence of scavengers, Cr_2O_3-G and Cr_2O_3-C achieved high efficiencies (95.9% and 95.7%, respectively). The introduction of isopropanol (•OH scavenger) reduced activity to 86.8% and 90.0%, while dimethyl sulfoxide (e^- scavenger) further lowered efficiencies to 78.1% and 81.4%. Ascorbic acid ($•O_2^-$ scavenger) suppressed activity to 74.6% and 80.9%, and the strongest inhibition was observed with ammonium oxalate (h^+ scavenger), dropping efficiencies to 52.1% and 56.8% (Fig. 19).

These results confirm that all ROS contribute to MB degradation, but photogenerated holes (h^+) dominate, followed by •OH, e^-, and $•O_2^-$. This trend aligns with previous studies on metal oxide-based photocatalysis [28, 33, 36]. Mechanistically, h^+ directly oxidizes MB and generates •OH through water oxidation, while conduction band e^- reduces O_2 to $•O_2^-$, enabling complementary degradation pathways.

4 Conclusions

Chromium oxide nanoparticles were successfully synthesized by both green and sol–gel methods, and their structural, optical, and photocatalytic properties were systematically compared. FTIR confirmed characteristic Cr–O stretching and bending vibrations, while XRD revealed a rhombohedral crystal phase with high crystallinity in both samples. Crystallite size analysis showed that green-synthesized Cr_2O_3 (38–48 nm) possessed smaller domains and higher specific surface area than sol–gel-derived Cr_2O_3 (44–58 nm). Optical studies indicated two band gaps (3.05–3.07 eV and 4.15–4.17 eV), attributed to size confinement and defect-related states, enabling absorption in both visible and UV regions. DLS and zeta potential analysis confirmed excellent colloidal stability of Cr_2O_3-G (−44.3 mV) compared to Cr_2O_3-C (−21.5 mV). SEM–EDX revealed distinct morphologies and compositions consistent with theoretical Cr_2O_3 stoichiometry. Photocatalytic tests showed superior dye degradation by Cr_2O_3-G, achieving 97% methylene blue removal at 10 ppm within 20 minutes, outperforming sol–gel Cr_2O_3 and reported catalysts in literature.

Data availability

No datasets were generated or analysed during the current study.

Author contributions All authors have participated in the research activities of this paper. AW, IM, FY, DA, AA, FB, and ANA, performed material preparation, data collection, and analysis. The first draft of the manuscript was written by AW and IM, and all authors have commented on previous editions. IM and DA revised the original manuscript. All authors read and approved the final manuscript.

Compliance with ethical standards

Conflict of interest The authors declare no competing interests.

Publisher's note Springer Nature remains neutral with regard to jurisdictional claims in published maps and institutional affiliations.

Open Access This article is licensed under a Creative Commons Attribution 4.0 International License, which permits use, sharing, adaptation, distribution and reproduction in any medium or format, as long as you give appropriate credit to the original author(s) and the source, provide a link to the Creative Commons licence, and indicate if changes were made. The images or other third party material in this article are included in the article's Creative Commons licence, unless indicated otherwise in a credit line to the material. If material is not included in the article's Creative Commons licence and your intended use is not permitted by statutory regulation or exceeds the permitted use, you will need to obtain permission directly from the copyright holder. To view a copy of this licence, visit http://creativecommons.org/licenses/by/4.0/.

References

1. Dihom HR, Al-Shaibani MM, Mohamed RMSR, Al-Gheethi AA, Sharma A, Khamidun MHB (2022) Photocatalytic degradation of disperse azo dyes in textile wastewater using green zinc oxide nanoparticles synthesized in plant extract: A critical review. J Water Process Eng 47:1–12.
2. Basumatary S, Kumar KJ, Daimari J, Mondal A, Kalita S, Dey KS, Deka AK (2023) Biosynthesis of silver nanoparticles using Antidesma acidum leaf extract: its application in textile organic dye degradation. Environ Nanotechnol Monit Manag 19:100769.
3. Gyawali N, Kandel R, Lee I, Shrestha S, Pandey A, Akter J, Hahn JR (2024) Silver decoration of Cr_2O_3 nanoparticles: Facile preparation of Cr_2O_3 nanoparticles and Ag– Cr_2O_3 nanocomposites and characterization of their antibacterial activity and ability to photocatalytically degrade organic wastes under visible light. J Photochem Photobio A: Chem 447:115251.
4. Cheema AN, Muneer I, Yasmeen F, Ali D (2025) Impact of niobium doping on photocatalytic degradation efficiency of iron

oxide nanoparticles for methylene blue dye under UV and sunlight. Mater Sci Eng: B 312:117878.
5. Maham I, Muneer AN, Cheema D, Ali F, Yasmeen (2024) Hydrothermal synthesis of Gd-doped CaO nanoparticles from lemon peel extract for efficient photocatalytic degradation of methylene blue under UV and sunlight. Ceram Int 50:54064–54075.
6. Nachiyar CV, Rakshi AD, Sandhya S, Jebasta NBD, Nellore J (2023) Developments in treatment technologies of dye-containing effluent: A review. Case Stud Chem Environ Eng 7:100339.
7. Algarni TS, Al-Mohaimeed AM (2022) Water purification by adsorption of pigments or pollutants via metaloxide. J King Saud Univ – Sci 34:102339.
8. Tahir MY, Sillanpaa M, Almutairi TM, Mohammed AA, Ali S (2023) Excellent photocatalytic and antibacterial activities of bio-activated carbon decorated magnesium oxide nanoparticles. Chemosphere 312:137327.
9. Khan S, Noor T, Iqbal N, Yaqoob L (2024) Photocatalytic Dye Degradation from Textile Wastewater: A Review. ACS Omega 9:21751–21767.
10. Rehman R, Uz-Zaman W, Abbas A, Mitu L (2019) Rapid photocatalytic degradation of methylene blue, tartrazine and brilliant green, dyes by high-flux UV irradiation photolysis reactor. Bulgar Chem Commun 51:337–341.
11. Fouedjou RT, Tsakem B, Noundou XS, Fogang HPD, Donkia AT, Ponou BK, Poka M, Demana PH, Teponno RB, Tapondjou LA (2023) Ethnobotany, Phytochemistry, and Biological Activities of the Genus Cordyline. Biomolecules 13:1783.
12. David SA, Doss A, Pole RP (2023) Biosynthesis of chromium oxide nanoparticles by Momordica charantia leaf extract: characterization and their antibacterial activities. Results Surf Interfaces 11:100120.
13. Duraivathi C, Jeya JP, Poongodi J, Johnson HJ (2022) Green synthesis of chromium oxide nanoparticles-study of its antibacterial, photocatalytic and thermodynamic properties. J Adv Sci Res 13:17–23.
14. Thakur TM, Lokhande RS, Thigle MM, Patil VR (2023) Nanoparticles of chromium oxide by green synthesis using Eucalyptus globulous leaves extract; characterization and biological activity studies. Mater Today: Proc 79:100–106.
15. Latha KP, Sundar SM (2020) Synthesis of chromium oxide nanoparticles at different PH and their structural and optical properties. J Eng Sci 11:111–122.
16. Cheah SY, Tey LH, Aminuzzaman M, Phang YK, Chan YB, Djearamane S, Watanabe A (2023) Green Synthesis and Characterizations of Chromium Oxide Nanoparticles (Cr_2O_3 NPs) Derived from Pomegranate Husk and its α-Amylase Inhibitory and Antioxidant Properties. Nano Hybrids Compos 39:51–55.
17. Farrukh MA, Butt KM, Chong KK, Chang WS (2019) Photoluminescence emission behavior on the reduced band gap of Fe doping in CeO_2-SiO_2 nanocomposite and photophysical properties,. J Saudi Chem Soc 23:561–575.
18. Badger RM (1935) The relation between the internuclear distances and force constants of molecules and its application to polyatomic molecules. J Chem Phys 3:710–714.
19. Ishtiaq M, Ali D, Ahmad R, Muneer I, Bashir F, Hanif M, Khan TM, Abbasi SA (2023) A comparison of antibacterial activity in dark-UV light in perspective of surface and structural properties of spray pyrolysis grown Cu doped Cr2O3 thin films. Surf Interfaces 37:102741.
20. Pinho PVB, Chartier A, Moussy JB, Menut D, Miserque F (2020) Crystal field effects on the photoemission spectra in Cr2O3 thin films: From multiplet splitting features to the local structure. Materialia 12:100753.
21. Ali D, Muneer I, Pirzada M, Ejaz T, Yasmeen F, Bashir F, Hanif M, Aziz MH, Wahab R (2025) Green-mediated sol-gel fabrication of CuO/ZnO nanoparticles from orange peel extract for environmental remediation: Insights from X-ray diffraction analysis using various models. Phys Scr 100:015980.
22. Ali D, Arooj N, Muneer I, Bashir F, Hanif M, Ali S (2023) Sustainable synthesis of ZnO nanoparticles from Psathyrella candolleana mushroom extract: Characterization, antibacterial activity, and photocatalytic potential. Inorg Chem Commun 158:111588.
23. Ali D, Muhammad N, Muneer I, Bashir F, Alam M, Haque AU (2025) Enhanced supercapacitive performance of wo3/bi2moo6 nanocomposite: synthesis, characterization, and electrochemical analysis. Ceram Int 51:32510–32521.
24. John KI, Adenle AA, Adeleye AT, Onyia IP, Amune-Matthews C, Omorogie MO (2021) Unravelling the effect of crystal dislocation density and microstrain of titanium dioxide nanoparticles on tetracycline removal performance. Chem Phys Lett 776:138725.
25. Khalaji AD (2021) Structural, Optical and Magnetic Studies of Cr_2O_3 Nanoparticles Prepared by Microwave-Assisted Synthesis. Nanochem Res 6:18–24. https://doi.org/10.22036/ncr.2021.01.003.
26. Anandan K, Rajendran V (2014) Studies on structural, morphological, magnetic and optical properties of chromium sesquioxide (Cr_2O_3) nanoparticles: Synthesized via facile solvothermal process by different solvents. Mater Sci Semicond Process 19:136–144.
27. Roy M, Ghosh S, Naskar MK (2015) Solvothermal synthesis of Cr_2O_3 nanocubes via template-free route. Mater Chem Phys 159:101–106.
28. Wahba MA, Abdelkader MMG, El-Mossalamy EH (2025) Tailoring Optical, Dielectric, and Magnetic Properties of Highly Efficient Visible-Light $LaFeO_3$ Photocatalysts via Ca/Ba Mono and Co-doping,. Mater Chem Phys 341:130916.
29. Liu H, Raza A, Aili A, Lu J, AlGhaferi A, Zhang T (2016) Sunlight-sensitive anti-fouling nanostructured TiO_2 coated Cu meshes for ultrafast oily water treatment. Sci Rep. 6:25414.
30. Balamurugan K, Mandal, S, Kumar NH, Santhosh PN, Magnetic and Optical Properties of Cr_2O_3 Nanoparticles, Proceedings of the DAE Solid State Physics Symposium (2007).
31. Rabeea MA, Owaid MN, Aziz AA, Jameel MS, Dheyab MA (2020) Mycosynthesis of gold nanoparticles using the extract of Flammulina velutipes, Physalacriaceae, and their efficacy for decolorization of methylene blue. J Environ Chem Eng 8:103841.
32. Adnan WG, Mohammed AM (2024) Green synthesis of chromium oxide nanoparticles for anticancer, antioxidant and antibacterial activities. Inorg Chem Commun 159:111683.
33. Wahba MA, Khaled RK (2025) V/Zn Incorporated-MCM-41: synthesis, characterization and visible light photocatalytic activity for tetracycline degradation. J Inorg Organomet Polym Mater 35:4445–4464.
34. Ogunlaja A, Nwankwo IN, Omaliko ME, Olukanni OD (2020) Biodegradation of methylene blue as an evidence of synthetic dyes mineralization during textile effluent biotreatment by Acinetobacter pittii. Environ Process 7:931–947.
35. Hameed TA, Yakout SM, Wahba MA, Sharmoukh W (2022) Vanadium-doped CuO: Insight into structural, optical, electrical, terahertz, and full-spectrum photocatalytic properties. Opt Mater 133:113029.
36. Wahba MA, Khaled RK, Enhanced, optical, and photocatalytic features of Gd-doped and Gd/Nd co-doped CoFe2O4 nanostructures, J Rare Earths 2025, https://doi.org/10.1016/j.jre.2025.06.007.
37. Khatamian M, Dastar E, Shokouhi SF, Nami SH (2023) Synthesis of pure nano Cr_2O_3 from chromite ore by a novel method and investigation of its composites with bentonite for their photocatalytic properties. J Iran Chem Soc 20:2805–2819.
38. Ali SQ, Aziz WJ, Kadhim DA, Abid MA, Sabry RS (2024) Corn plant leaf extract inhibits microbial growth with the photocatalytic activities of MB, MO, and RdB dye-mediated nano- Cr_2O_3. Nano-Struct Nano-Objects 39:101257.

39. Fatima E, Arooj I, Javeed M, Yin J (2024) Green synthesis, characterization and applications of Phyllanthus emblica fruit extract mediated chromium oxide nanoparticles. Discov Nano 19:68.
40. Vanithaa G, Manikandan R, Prakasam A, Navinkumar MD, Sathiyamoorthi K, Dhinakaran B (2022) Photo-degradation of four different organic dyes in green synthesized chromium nanoparticles by leaf extracts of Ocimum basilicum - Lamiaceae (Thiru Neetru Pathilai). PG Res Dep Phys Gov Arts Coll 21:1–10.
41. Yadav S, Rani N, Saini K (2023) Synthesis and characterization of NiO/ Cr_2O_3 nanocomposite with effective sunlight driven photocatalytic degradation of organic dyes,. Environ Sci Pollut Res 30:71957–71969.
42. Helal A, Harraz FA, Ismail AA (2021) One-step synthesis of heterojunction Cr_2O_3 nanoparticles decorated Bi_2S_3 nanorods with enhanced photocatalytic activity for mineralization of organic pollutants. J Photochem Photobiol A: Chem 419:113468.